

Experimental Testing and Computational Simulation of Helicopter Blade Twist Actuation By Means of Piezoelectric Actuation

Guilherme da Costa Duarte
Guilherme.c.duarte@tecnico.ulisboa.pt

Instituto Superior Técnico, Universidade de Lisboa, Portugal

June 2018

Abstract

This work is focused on the implementation of blade twist by piezoelectric actuation, targeted at helicopter blades, by employing Macro fiber composite (MFC) actuator patches at $\pm 45^\circ$ inclination relative to blade span. First, the actuation behaviour of the MFC is tested in a simple setup, referred to as the unimorph. This system is modelled and analysed using the Ritz method, as well as by a Finite element method (FEM) simulation, and compared with experimental measurements. With a fair correlation achieved between the three methods, the more complicated system of the blade is created. A model scale helicopter blade is then designed and manufactured by 3-D printing. Tensile tests are performed to assess the effect the manufacturing method has on the properties of the PETG material used for the blade, the results of which show the Young's modulus, yield and ultimate strength all to be considerably lower than the documented values. A non-linear static FEM simulation is then performed on the blade model taking into account gravity and centrifugal forces on top of the piezoelectric actuation. Experimental measurements of the deflection of the trailing edge due to actuation are taken. Both methods show the MFC actuators generating constant rate of twist along their length with similar maximum actuation values, but the values diverge at the blade tip. Finally, larger scale FEM simulations were created to estimate the possible actuation on real-life systems.

Keywords: Piezoelectric actuator, MFC, Helicopter blade twist, Experimental methods, Finite element method,

Nomenclature

α^T	Coefficients of Thermal Expansion.
γ	Engineering shear strains.
ε	Infinitesimal Strain.
ν	Poisson's Ratio.
Π	Total Potential Energy.
σ	Stress.
φ	Ritz Approximation Functions.
C	Elasticity Tensor.
c^r	Ritz Coefficients.
d	Piezoelectric Constants.
\mathcal{E}	Electric Field.
E	Young's Modulus.
e	Piezoelectric Modulus.
E^G	Green-Lagrange finite strain tensor.
$h_{electrodes}$	Distance Between Electrodes.
Q	Reduced Stiffness Matrix.

S	Compliance Tensor.
T_c	Current Temperature.
U	Internal internal strain energy of the elastic body.
u	Displacement Component in the x Direction.
V	Electric Potential.
v	Displacement Component in the y Direction.
V^{ext}	External Forces Potential.
w	Displacement Component in the z Direction.
x, y, z	Cartesian Coordinate System.

1. Introduction

The blades of the helicopter face different aerodynamic environments along their span (almost stationary close to the hub and sonic at its tip), and because of this, one important factor influencing main rotor performance is blade twist. Because the optimum blade twist depends on the flight conditions,

the twist built into the modern helicopter blade focuses only on the optimization of the flight condition most important to the mission profile [1].

However, with the development of smart materials allowing the blade to alter itself during flight, the prospect of achieving the optimum blade twist for all flight conditions has become an interesting goal. With this intent, Lonoce [2] performed a blade element theory based study of several twist distributions on the Sikorsky UH-60A Black Hawk helicopter, in order to calculate the optimum twist for different forward speeds (or rather, advance ratios). That work concluded that a linear distribution along the middle section of the blade span would provide a power consumption reduction of 6.09% . Between hover and 0.35 advance ratio, a $-1^\circ/\text{m}$ (defined negative for nose down) actuation across the middle section would be required for this effect.

1.1. Piezoelectricity

For their ability to transform electric energy into displacement and viceversa, it is of no wonder that piezoelectric materials have been used in a wide range of applications. Piezoelectric materials can be used as sensors to scan for damage in structures [3], or as energy harvesters [4], or as surgical equipment [5], or - more relevant to this work - as actuators for smart structures. Wilbur et al. [6] used piezoelectric actuators to counteract rotor vibrations on the NASA active twist rotor. A reduction in fixed system loads of 60% to 95% depending upon flight conditions was registered, with 1.1° to 1.4° of blade twist. Piezo actuators have also been useful in micro air vehicle applications with Dwarakanathan et al. [7] successfully using a piezoelectric morphed trailing edge as elevons, and Bilgen [8] showing the piezoelectric-actuated variable camber airfoil produced lower drag. Bilgen [9] would later on use piezoelectric actuators again to delay flow separation, recording a maximum lift coefficient increase of 27.5% at a frequency of 125 Hz.

Piezoelectric actuators can take many forms, from the classic monolithic ceramics and stacked versions thereof, to mechanically amplified actuators [10], or shear-mode actuators [11] or the Macro Fiber Composite (MFC) actuators [12]. Among these options, the MFC stood out as the better choice and is the one used in this work, as well as many of the aforementioned actuator applications.

1.1.1 The Macro Fiber Composite

Active Fiber Composites (AFC) were first developed at MIT throughout the 90s, with the objective of surpassing the shortcomings of monolithic piezoceramics, such as the lack of flexibility and conformability to structures. With this intent, the

AFC was created as a thin actuator sheet that could easily be bent without becoming compromised.

The modern MFC is made up of a central layer of machined PZT fibers surrounded by an epoxy matrix. This central active layer is sandwiched between layers of polyimide (Kapton) film, etched with the electrode pattern. A schematic of the modern MFC structure can be seen on Figure 1.

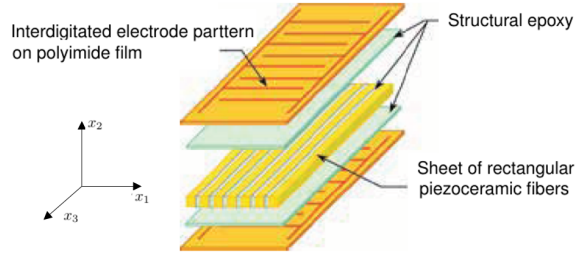


Figure 1: Structure of the MFC (adapted from [12])

2. Theoretical Fundamentals

2.1. Constitutive equations

For most materials, only the relation between the stress and strain is needed (at isothermal conditions) in their constitutive equations. However, the constitutive equation of any piezoelectric material requires another term to be added to represent the influence of the electric field on the stress of the material [13]:

$$\sigma_{ij} = C_{ijkl}\varepsilon_{kl} - e_{ijk}\mathcal{E}_k \quad , i, j, k, l = 1, 2, 3 \quad (1)$$

where σ_{ij} are the components of the stress tensor, C_{ijkl} are the elastic moduli, ε_{kl} are the components of the strain tensor, e_{ijk} are the piezoelectric moduli, and \mathcal{E}_k are the components of the electric field. Since the piezoelectric moduli, e are not usually provided by the manufacturer of the actuator, it is often used the inverse constitutive relation instead:

$$\varepsilon_{ij} = S_{ijkl}\sigma_{kl} + d_{ijk}\mathcal{E}_k \quad , i, j, k, l = 1, 2, 3 \quad (2)$$

where d_{ijk} are piezoelectric constants and S_{ijkl} are the components of the compliance tensor.

2.2. Thermal analogy

For the FEM simulations performed throughout this work, the software *Siemens NX* has been used. However, since *Siemens NX* software is not able to directly take into account the piezoelectric characteristics of materials, but can simulate the thermal expansion of materials, the piezoelectric effect can be recreated instead through a thermal analogy. This is done by changing one term in Eq.(2):

$$d_{ijk}\mathcal{E}_k = \alpha_{ij}^T(T_c - T_0) \quad (3)$$

where α_{ij}^T are the coefficients of thermal expansion, T_c is the current temperature and T_0 is the reference temperature.

Assuming a constant electric field generated by two parallel electrodes, it follows that the through thickness electric field is related to the applied electric potential by [14]:

$$\mathcal{E}_i = -\frac{\partial V}{\partial x_i} = \frac{V_2 - V_1}{h_{electrodes}} \quad (4)$$

where V is the electric potential and $h_{electrodes}$ is the distance between electrodes. Combining Eq.(3) and (4) and equating only the constants (removing the inputs voltage and temperature) the thermal expansion coefficient can be calculated:

$$\alpha_{ij}^T = \frac{d_{ijk}}{h_{electrodes}} \quad (5)$$

The electrode spacing can be calculated based on the free strain provided by the manufacturer (Table 1) [7]:

$$h_{electrodes} = \frac{V_{max}d_{333}}{\varepsilon_{free}} \quad (6)$$

From Eq.(6), for 1500V maximum voltage and 1400ppm free strain the assumed electrode spacing becomes $493\mu\text{m}$. In Table 1 can be seen the values of thermal expansion coefficient obtained.

Table 1: Piezoelectric constant[12] and Thermal expansion coefficients.

constant	High-Field	Low-Field
d_{333}	460pm/V	400pm/V
d_{113}	-210pm/V	-170pm/V
α_{333}	9.33e-7 m/ $^\circ$	8.11e-7 m/ $^\circ$
α_{113}	-4.26e-7 m/ $^\circ$	-3.45e-7 m/ $^\circ$

2.3. Strain-Displacement Equations

For any deformable body, the strain-displacement relations are found by considering the change in distance between two infinitesimal close points in the body. For this general case the Green-Lagrange strain tensor can be written as:

$$E_{ij}^G = \frac{1}{2} \left(\frac{\partial u_i}{\partial x_j} + \frac{\partial u_j}{\partial x_i} + \frac{\partial u_k}{\partial x_i} \frac{\partial u_k}{\partial x_j} \right), \quad i, j, k = 1, 2, 3 \quad (7)$$

where u_i are the displacement components of any material in the x_i orthogonal directions. These

non-linear strain-displacement equations are seldom used in their full form, with different simplifications allowing the higher order terms to be neglected. When the composite plate is under small strains but moderate rotations ($\sim 10^\circ - 15^\circ$), it is a good approximation to neglect all quadratic terms of the non-linear strain not related to rotations of the transverse normals, that is to say all quadratic terms but for $\left(\frac{\partial w}{\partial x}\right)^2$, $\left(\frac{\partial w}{\partial y}\right)^2$, $\frac{\partial w}{\partial x} \frac{\partial w}{\partial y}$.

2.4. Classical Laminated Plate Theory

For the unimorph used later in this work it is possible to apply the Classical laminated plate theory (CLPT), since it fulfils its several restrictions. By applying the CLPT, the Kirchhoff hypotheses is assumed [15].

As a result of these assumptions, the state of plane strain is implied such that the transverse normal and shear strains equal zero: $\varepsilon_{zz} = \varepsilon_{yz} = \varepsilon_{xz} = 0$. It follows from Kirchhoff hypotheses that the displacements take the following form:

$$\begin{aligned} u(x, y, z, t) &= u_0(x, y, t) - z \frac{\partial w_0}{\partial x} \\ v(x, y, z, t) &= v_0(x, y, t) - z \frac{\partial w_0}{\partial y} \\ w(x, y, z, t) &= w_0(x, y, t) \end{aligned} \quad (8)$$

This allows to reduce the study of a 3-D plate to the study of its midplane, a 2-D problem where the displacements of any point in the 3-D plate can be known from Eq.(8), simply by knowing the displacements on the midplane.

Replacing the displacement field from Eq.(8) into Eq.(7) and applying the simplifications from small strains and moderate rotations, finally the von Kármán strain are obtained:

$$\begin{Bmatrix} \varepsilon_{xx} \\ \varepsilon_{yy} \\ \gamma_{xy} \end{Bmatrix} = \begin{Bmatrix} \frac{\partial u_0}{\partial x} + \frac{1}{2} \left(\frac{\partial w_0}{\partial x} \right)^2 \\ \frac{\partial v_0}{\partial y} + \frac{1}{2} \left(\frac{\partial w_0}{\partial y} \right)^2 \\ \frac{\partial u_0}{\partial y} + \frac{\partial v_0}{\partial x} + \frac{\partial w_0}{\partial x} \frac{\partial w_0}{\partial y} \end{Bmatrix} + z \begin{Bmatrix} -\frac{\partial^2 w_0}{\partial x^2} \\ -\frac{\partial^2 w_0}{\partial y^2} \\ -2 \frac{\partial^2 w_0}{\partial x \partial y} \end{Bmatrix} \quad (9)$$

where γ_{xy} are the engineering shear strains and equal to $2\varepsilon_{xy}$. With Eq.(9), the strain from any point on the entire laminate can be obtained simply from the strains of the midplane.

2.5. Ritz Method

The Ritz method is based on the principle of minimum total potential energy, which is variational form of the differential equations meant to

be solved. The Ritz method is then used to approximate a dependent unknown by a finite linear combination of coefficients and approximation functions [15].

In short, the principle of minimum total potential energy states that:

$$\partial(U + V^{ext}) = \partial\Pi = 0 \quad (10)$$

where U is the internal strain energy of the elastic body, V^{ext} is the potential associated with the work done by external forces applied to the body (and thus it is usually negative) and Π is the total potential energy. The form by which the value of these terms is obtained is later presented in section 4.1 in Eq.(15).

In this framework, the unknowns of the total potential energy are the displacements which are approximated by a linear combination of approximation functions, as follows:

$$u \simeq \sum_{j=1}^N c_j^r \varphi_j \quad (11)$$

where c^r and φ are the aforementioned Ritz coefficients and approximation functions respectively. The approximation functions must be chosen beforehand to best fit the expected solution and such that (at least) the geometric conditions are satisfied, while the coefficients of the problem are calculated by minimizing the derivative of Π with respect to each of the coefficients. In doing this, a system with equal number of equations and unknowns, N , is created. Solving the system and replacing the obtained coefficients back into Eq.(11) yields the approximate solution to the problem.

3. Experimental Set-up and Method

3.1. The Voltage Amplifier Circuit

The MFC actuator requires electric tension ranging from -500V to 1500V to operate, making it necessary to include a voltage amplifier in the control circuit. For this purpose, the voltage amplifier chosen was the *AMD2012-CE3* from *Smart Material Co.*. The variable output is controlled by the "CTL" input with two linear slopes. An input from 0V to 2.5V is amplified from 0V to 500V, and 2.5V to 5V input is amplified from 500V to 2000V at a steeper slope. Together with a fixed 500V bias, the full voltage range from -500V to 1500V is achieved. The amplifier circuit comes with an enable line such that a switch can be installed.

3.2. Measurement Method

The actuations in this work were measured with a digital calliper with a precision of 0.01mm, although, by calculating the absolute average deviation of the results, the uncertainty of the experiments was concluded to range from 0.07mm to

0.01mm, depending on the experiment, due to the human element. In the first set of experiments, the unimorph was clamped by a vise with another vise set perpendicular holding the calliper as shown on Figure 2. For the second set of experiments, the blade was clamped to an edge of the table while a track was clamped underneath that edge of the table where the calliper was secured. This track allows for the calliper to be positioned at different distances from the blade root, which were signalled in a ruler positioned between the blade and the track. A picture of this experimental assembly can be seen in Figure 3.



Figure 2: Unimorph grip and calliper assembly



Figure 3: Actuated blade and calliper assembly

The actuators were numbered from 1 to 4 and two methods of measurement were employed. The first method alternated between the maximum actuation and unactuated, registering measurements at those two stages. The second method also goes to full actuation and then unactuated, but goes to maximum negative actuation (-500V causing contraction of the MFC) before returning to unactuated, and measurements are taken at the maximum and at both unactuated stages.

4. Unimorph Actuator

A unimorph actuator consists of a M-4010-P1 MFC actuator bonded to a host with the same

length and width such that when tension is applied the actuator bends. The simplicity of the unimorph allows for the creation of an analytical model that can be compared with computational and experimental results.

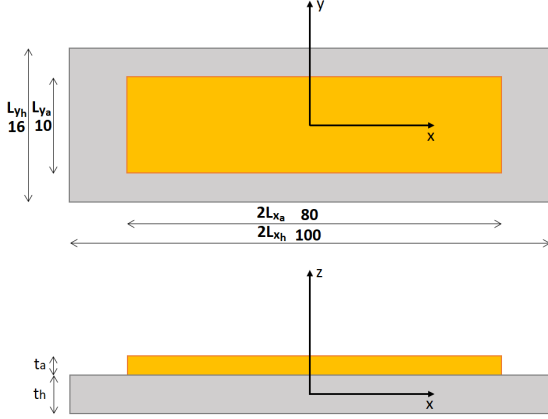


Figure 4: Unimorph dimensions and reference axis

4.1. Analytical Model

The analytical model is an application of the Ritz method presented in section 2.5. The approximation functions chosen are presented in Eq.(12) and have been used before in similar applications [8, 16].

$$\begin{aligned} u_0 &= c_3^r x - \frac{c_1^r x^3}{6} - \frac{c_1^r c_2^r x y^2}{4} \\ v_0 &= c_4^r y - \frac{c_2^r y^3}{6} - \frac{c_1^r c_2^r x^2 y}{4} \\ w_0 &= \frac{1}{2}(c_1^r x^2 + c_2^r y^2) \end{aligned} \quad (12)$$

In order to simulate the clamped end of the unimorph, it had to be considered for the Ritz method an actuator with double the length so that the clamped boundary conditions is fulfilled by symmetry of the deformed shape. The width of the actuator remains the same. The total potential energy for the unimorph is given by the sum of the total potential energy of the host and the total potential energy of the actuator under an electric field. For the host, the total potential energy is given by Eq.(13) and, since it is under no external forces, Eq. (13) corresponds only to the internal strain energy of the host.

$$U_h = \frac{1}{2} \int_{-L_{x_h}}^{L_{x_h}} \int_{-\frac{L_{y_h}}{2}}^{\frac{L_{y_h}}{2}} \int_{-\frac{t_h}{2}}^{\frac{t_h}{2}} [\sigma_h \cdot \varepsilon] dz dy dx \quad (13)$$

The material chosen for the host was aluminium, making the host's constitutive relation the following:

$$\begin{Bmatrix} \sigma_{xx_h} \\ \sigma_{yy_h} \\ \gamma_{xy_h} \end{Bmatrix} = \frac{E}{1-\nu} \begin{bmatrix} 1 & \nu & 0 \\ \nu & 1 & 0 \\ 0 & 0 & \frac{(1-\nu)}{2} \end{bmatrix} \begin{Bmatrix} \varepsilon_{xx} \\ \varepsilon_{yy} \\ \gamma_{xy} \end{Bmatrix} \quad (14)$$

The strains are obtained by combining the approximations functions from Eq.(12) into Eq.(9) and are the same for the actuator and host, since a perfect bond is assumed.

For the actuator, the total potential energy is given by

$$\begin{aligned} \Pi_a &= \frac{1}{2} \int_{-L_{x_a}}^{L_{x_a}} \int_{-\frac{L_{y_a}}{2}}^{\frac{L_{y_a}}{2}} \int_{\frac{t_h}{2}}^{\frac{t_h}{2}+t_a} [(\sigma_a \cdot \varepsilon) \\ &\quad - (\sigma_{piezo} \cdot \varepsilon)] dz dy dx \end{aligned} \quad (15)$$

And the constitutive relation for the piezoelectric actuator is given by Eq.(1). For plane stress however, the term $-e_{ijk} \mathcal{E}_k$ representing the piezoelectric stress can be instead written in terms of the reduced stiffness matrix, the piezoelectric constants and the electric field as $-Q d_{ijk} \mathcal{E}_k$ [13].

$$\begin{Bmatrix} \sigma_{xx_a} \\ \sigma_{yy_a} \\ \gamma_{xy_a} \end{Bmatrix} = \begin{bmatrix} \frac{E_x}{1-\nu_{xy}\nu_{yx}} & \frac{\nu_{xy}E_y}{1-\nu_{xy}\nu_{yx}} & 0 \\ \frac{\nu_{xy}E_2}{1-\nu_{xy}\nu_{yx}} & \frac{E_y}{1-\nu_{xy}\nu_{yx}} & 0 \\ 0 & 0 & G_{xy} \end{bmatrix} \begin{Bmatrix} \varepsilon_{xx} \\ \varepsilon_{yy} \\ \gamma_{xy} \end{Bmatrix} - \begin{bmatrix} \frac{E_x}{1-\nu_{xy}\nu_{yx}} & \frac{\nu_{xy}E_y}{1-\nu_{xy}\nu_{yx}} & 0 \\ \frac{\nu_{xy}E_2}{1-\nu_{xy}\nu_{yx}} & \frac{E_y}{1-\nu_{xy}\nu_{yx}} & 0 \\ 0 & 0 & G_{xy} \end{bmatrix} \begin{Bmatrix} d_{xxx} \\ d_{yyx} \\ 0 \end{Bmatrix} \mathcal{E}_x \quad (16)$$

Solving the integrals and summing the contribution to the total potential energy from the host and the actuator results in a non-linear function of the four constants present in the approximation functions in Eq.(12). This function must then be derived with respect to each of the constants so that a four equations, four unknowns non-linear system is obtained.

4.2. Computational Methods

In order to solve this system, a *matlab* script was created. This script allows for the input of all the material constants, as well as the dimensions of the unimorph, calculates the total potential energy integrals and finally solves the non-linear system, outputting the values of the four constants that minimize the total potential energy. It then uses those values to calculate the mid-plane deformations of the unimorph from Eq.(12). It does these tasks in a loop in order to calculate the displacements for

different host thickness in intervals of 0.01mm up to 1mm.

Having completed the Ritz analysis of the problem, a FEM simulation was performed with the *Siemens NX* software. In order to best match the Ritz analysis, the full double length actuator was simulated with the same reference axis seen in Figure 4. Both the host and actuator meshes employed CQUAD8 2-D elements and the material orientation for the actuator was set in the x direction. For boundary conditions, the host is clamped along the y axis while for the loads, a 1500° thermal load is applied to all the nodes on the actuator mesh. Several such simulations were run for host thickness ranging from 0.1 to 1mm in equal intervals of 0.1mm.

4.3. Experimental work

Two Unimorphs were tested, one with a 0.1mm thick aluminium host and another with a 0.8mm thick host. After the actuators have been properly bonded with the hosts, the deflection measurements are performed with the same two methods as described in section 3.2, with fifteen cycles being performed.

4.4. Results

The results for both the Ritz analysis, *Siemens NX* simulation and experimental measurements can be seen on Figure 5.

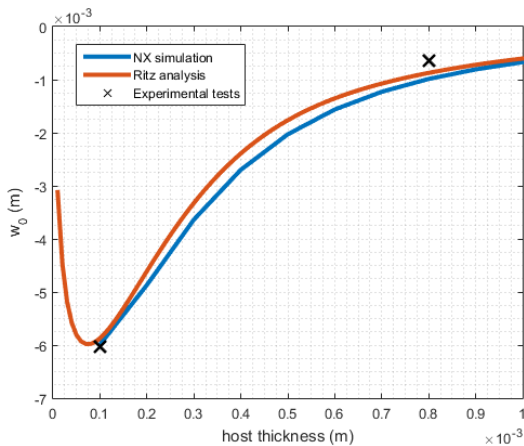


Figure 5: Maximum w_0 displacements for different host thickness

It can be observed that both the Ritz results and the FEM simulation closely follow the same tendency with the largest difference being of 15.4% for a host thickness of 0.6mm. The black crosses mark the averages of the measured values. For the host thickness of 0.1mm there is excellent correlation with the *Siemens NX* values with only a 0.5% (0.03mm) difference. For the 0.8mm host thickness the difference is 35.2% (0.35mm) but it should be

noted that preliminary experiments with removable bounds hinted at the actuator used in the 0.8mm unimorph having below average actuation characteristics.

5. Actuated Blade

5.1. Blade design

As this work follows up on the blade twist optimization for the Sikorsky UH-60A helicopter [2], its blade was taken as a baseline and the scaling of it was attempted under the several constraints present.

5.1.1 Sizing restrictions

While scaling of wings usually focus on matching the Reynolds number to suitably scale aerodynamic behaviour, doing so in helicopter blades becomes problematic as it will require the rotor speed to increase by the square of the inverse of the geometric scale if testing on air [17].

Because of the difficulties in matching Reynolds number, helicopter scaling instead focuses on matching the Mach number, as this allows to duplicate compressibility effects at the blade's tip and also has lower requirements than matching the Reynolds number, only requiring the rotor speed to increase linearly with the inverse of the geometric scale. Another important factor in helicopter blade scaling is the Lock number, which is the ratio between the aerodynamic forces and the inertial forces. It affects directly the blade flapping angles and is important to match rotor loads and predict the blade stability [17]. It does not depend on the rotor speed, but instead, the blade mass per unit length has a great influence on its value.

The first constraint was the size of the actuator available, as it limits the chord size. It must be positioned at 45° for maximum actuation [6] which, leaving 10% of the chord uncovered at each edge, requires a chord of approximately 59mm.

As this blade was created with the intent of possible further work in a wind tunnel, the size of the available facility imposes the second constraint: the rotor radius cannot exceed 0.679m.

The final constraint considered was the material limits. It was decided that the blade would be 3-D printed in PETG. A 3-D printing service was hired to print the blade, as its dimensions surpassed the limits of the 3-D printers available at Instituto Superior Técnico. The printing service advised the blade to be done with a 20% infill and a $250\mu\text{m}$ filament. Because the documented values for the material properties of the PETG don't represent the strength that can be expected from materials that are 3-D printed, tensile tests were performed to establish the Young's modulus of the printed PETG as well as their yield strength. A total of twelve test specimens were printed, divided into sets of four

with each set being printed in a different direction (the layers of material were deposited in planes perpendicular to the printing direction).

The tensile tests were performed on an *Instrom 5566* mechanical testing machine at a speed of 2mm/min, while the load was measured by the testing machine and a strain gauge mounted on the test specimen measured the axial strain. As there was no transversal strain gauge available, a Poisson's coefficient of 0.37 (from PET material [18]) was used to calculate the change of test section area (from its original 6mm by 12mm) and calculate the and true stress. The machine registered the load at yield based on a 2% offset as well as load at fracture. The results gathered were then compiled into a stress-strain curve such that the slope of the linear section could be calculated and this slope gives the Young's modulus of the material.

Table 2: Tensile test results [MPa]

Specimen	Yield Stress	Young's Modulus
X average	8.053	705.870
Y average	9.579	683.148
Z average	8.941	622.758

All results are considerably lower than the documented values. However, in spite of the different printing direction, the Young's modulus does not vary much between test subjects and, therefore, the behaviour of the PETG has been considered isotropic for the FEM simulation, with a Young's modulus of 670.592MPa. With these values for the PETG yield strength, it became woefully apparent that it could not withstand the centrifugal loads caused by the rotor speed required to match the Mach number.

5.1.2 Final design choice

With all the constraints present in this work, the goal of testing a scaled blade had to be forgone altogether, and the rest of this work is directed at achieving correlation between the FEM simulation and experimental results.

With all the compromises in mind, the design of the final blade is summarized in Table 3. The airfoil was replaced for the NACA0012 since its larger thickness allowed for a larger safety margin should dynamic tests be attempted.

5.2. NX simulation

The blade model can be seen on Figure 6 along with a model of the hub, which, despite having been modelled, is not meshed and is not taken into account on the simulation.

¹Given as a fraction of main rotor radius

Table 3: Test blade parameters

Main rotor radius	0.585 [m]
Blade chord length	0.059[m]
Blade root offset ¹	0.145
Airfoil	NACA0012
Blade mass per unit length	0.412[kg m ⁻¹]
Section lift coefficient slope [19]	6.385 [rad ⁻¹]

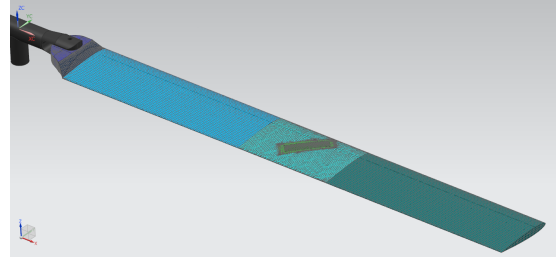


Figure 6: Blade assembly modeled in NX software

From the colors of the image, it can be seen that the blade is split into five regions, not counting the actuators, which are a different body from the blade. This was done in order to apply different meshes to each to better match their geometry. The actuators were modelled in two parts, for the active and passive regions of the MFC actuator, and are positioned in a slot created into the blade to house them and position them at the desired $\pm 45^\circ$ (although not visible from the image, the bottom actuator is positioned perpendicular to the top one). The actuators were meshed by a 2-D mesh of CQUAD8 quadrilateral elements. The grip region of the blade was composed of a swept mesh from top to bottom of CHEXA20 six sided solid elements. The transition from the grip to the blade is done with CTETRA10 tetrahedral elements in order to easily follow the transition. The middle airfoil section is meshed by a tetrahedral mesh and it includes actuator slots that alter its cross section, making it impossible to create a swept mesh across. The remaining airfoil sections (left and right of the section with the actuators) have identical CHEXA20 meshes swept span-wise.

Entering the simulation stage, the contact conditions as well as the loads and constraints are defined. Glue contact conditions are defined between the bottom surfaces of the actuator and the faces of the corresponding slots on the blade and their bond is assumed perfect. The constraints applied fixed the bottom and top surfaces of the grip section of the blade. In order to simulate the thermal, gravity and centrifugal loads in a non-linear simulation, several increments of the target loads were divided into substeps of the solution in order to help

it converge. The last two substeps of the solutions were the unloading of the thermal load in the same increments but with a constant gravity or centrifugal load. This allows for results to be registered with only the actuation, or with the actuation and gravity/rotation, or only with gravity/rotation. By comparing the results it can be seen how such forces should affect the actuation.

5.2.1 Results

In Tables 4 and 5, the blade twist at the tip of the blade (defined positive for nose down twist) for different loading conditions can be seen as well as the difference between the case with the thermal and gravitic/centrifugal loads and with only the gravitic/centrifugal load. The results show that these two forces can be summed linearly without influencing each other, made evident by the fact that removing the twist caused by only the load (C/G) from the solution with the load and actuation (T+C/G) results in the twist produced by only the actuation (T).

Table 4: Blade twists $[\circ]$ for a 1000° thermal (T) load combined with gravity (G) and rotation (C)

T	G	T+G	C	T+C
0.2948	-0.0886	0.2061	-3.1966	-2.9014
-	T+G - G		T+C - C	
-	0.2947		0.2952	

Table 5: Blade twists $[\circ]$ for a 1500° thermal load (T) combined with gravity (G) and rotation (C)

T	G	T+G	C	T+C
0.4421	-0.0886	0.3535	-3.1966	-2.7538
-	T+G - G		T+C - C	
-	0.4421		0.4428	

5.3. Experimental work

With the actuators bonded, the blade was ready for testing. The measuring set-up was mounted (Figure 3) with several markings along the span of the blade. Measurements were taken on twelve different positions along the blade span at a distance of 235, 285, 310, 320, 335, 350, 360, 385, 435, 485, 535, 585 (mm) from the blade root. The actuators were positioned between 310 mm and 360 mm. On each of these twelve positions, fifteen measurements cycles were performed, except for the positions where the actuation was non-existent, performing only five cycles then.

5.3.1 Results and comparison

The averages of the maximum deflection of the trailing edge are compared with results from the Siemens NX FEM simulation in Figures 7 and 8.

Firstly, it can be seen that the actuation is linear in the sense that for a load of two thirds, the actuation is also two thirds. It is also linear in the sense that it increases linearly across the section of the blade which has the actuator embedded, without twisting the sections of the blade before or after. This is in line with the actuation objectives laid out by [2], where a linear twist in the middle section of the blade was required. The rate of twist this actuation represents is $5.90^\circ/\text{m}$ for 1000V and $8.84^\circ/\text{m}$ for 1500V and while these may seem very promising values, they are a consequence of the small dimensions of the blade as well as its flexible material.

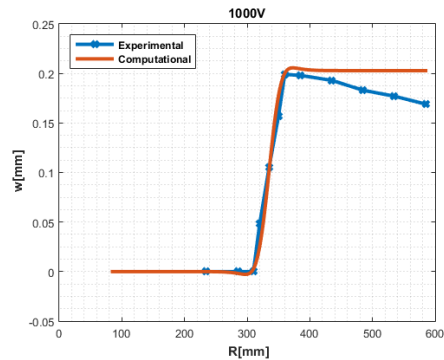


Figure 7: 1000V results comparison

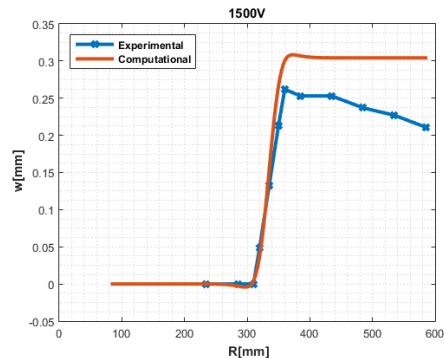


Figure 8: 1500V results comparison

In both cases, the measured actuation has a fair correlation with the expected from the FEM simulation. For the 1000V case, the experimental measurement, at the point of maximum actuation (360mm) there is an excellent correlation reaching 98.2% of the FEM expectation. For the 1500V case, however, this correlation is weaker, reaching at its peak only 86.2% of the computational value. What is most discrepant between the measurements and the simulation is the behaviour after the section that is actuated. While the simulation predicted the twist to remain constant, even when the effects

of other loads were combined, there is on both cases of the experimental measurements a noticeable decline in the actuation until the blade tip. For the 1000V case this decline equals 14.9% of the maximum actuation measured, while for the 1500V case it equals 19.5%.

5.4. Larger scale simulations

Although Mach scaling of the blade was not possible, having obtained a fair correlation between the FEM simulation and experimental results, it is possible to perform larger scale simulations and expect some real designs correspondence.

The first simulation performed was on a blade ten times larger than the model tested, with proportional actuators. This blade becomes of dimensions similar to full scale, but with a short radius. The preparation procedure was identical to the one performed in section 5.2.

For the second simulation performed, the blade was the same with the only difference being the actuator. While for this work, the actuator used had its fibres oriented along its length, which meant the actuators themselves had to be oriented at $\pm 45^\circ$, there are other actuators available that have their fibers already oriented at $\pm 45^\circ$, such as the M-8528-F1 MFC actuator. These can follow the span of the blade such that more surface area is actually actuated. In accordance with the requirements laid out by Lonoce [2], the blade was actuated from $0.5R$ to $0.85R$.

For the third simulation, the same 45° actuator was simulated, but the blade was changed altogether. While in this work, the model blade had a uniform cross-section made up of one single material, the UH-60A blade is made up of a titanium spar surrounded by a honeycomb structure and wrapped by a fiber-glass skin, together with a nickel plated leading edge [20]. In order to better estimate the amount of actuation expected in a real helicopter blade, this more complicated structure (Figure 9) has been simulated, albeit without the nickel plating, on a blade with the dimensions of the UH-60A blade.



Figure 9: Simulated UH-60A blade structure

For this third simulation, the mesh created was also made up of CHEXA20 elements swept across its span, although three separate meshes had to be created for the spar, the interior and the skin. For all three of these simulations only the thermal load was applied, and the simulation was linear static.

The blade twist and blade rate of twist obtained for all three cases can be seen on Table 6 (defined positive for nose down twist). As expected, the rate of twist achieved by actuation is considerably smaller than the rate obtained for the small scale cases. Comparing the first two cases, it can be seen that the second setup produces four times the rate of twist. This was also expected, as the second simulation actuated a much larger surface of the blade. The blade rate of twist obtained in the second simulation is actually enough to fulfil the requirements for optimization studied by Lonoce [2], of $-1^\circ/\text{m}$ rate of twist. However, this results is not realistic, as the material simulated was still the very flexible PETG. Comparing with the more representative third simulation, the rate of twist drops tenfold, bellow useful values for blade twist optimization, although some performance improvement may still be attainable bellow optimum performance.

Table 6: Larger scale twist results

Simulation	First	Second	Third
Twist [$^\circ$]	0.1632	2.1281	0.3254
Rate of twist [$^\circ/\text{m}$]	0.3130	1.2144	0.1373

6. Conclusions

This work set out to achieve twist actuation by means of piezoelectric actuation, and correlate values of physical measurements with computational FEM simulations with the intent of reaching the blade twist objective as laid out in [2].

First, an analytical model (Ritz) was compared with a FEM simulation and experimental results on a simple piezoelectric problem. The correlation between analytical and FEM results was fair, with a 15.4% difference at the most. The experimental measurements had mixed results. One of the tests had a near perfect match with the simulated results with only a 0.5% difference, whereas the other had a worrying 35.2% difference (Fig. 5). While this may seem very problematic at first, it should be noted that actuator in question seemed to be bellow average in capabilities (as inferred from preliminary experiments).

Secondly, the Mach scaling of the original UH-60A blade was attempted, but ultimately failed. The several constraints put on this work - actuator size, test space, available material - did not allow a semblance of scaling. With the actuated blade built under the present constraints, the work continued with the purpose of matching simulation results with experimental results and characterising the actuation created by the MFC actuators. Having recognised that the manufacturing process

of the blade heavily influenced the properties of its material, tensile tests were performed to better characterize the 3-D printed material. It was without much surprise that those properties were found to be considerably weaker than documented. The printed blade was more flexible than expected and also had a much lower yield strength (approximately a fifth) of the documented. With the material properties better defined, a non-linear static simulation of the actuated blade was run in the *Siemens NX* software to simulate not only the piezoelectric actuation but also the gravity and rotation affecting the blade. The results showed a linear blade actuation that was independent from other forces (tables 4, 5). It also showed a blade rate of twist that was deceptively high due to the small proportions of the blade. Finally, the experimental measurements of the actuation of the blade were undergone. Here, good correlation with the computational values was achieved, verifying the linear actuation. The value of the maximum actuation also reasonably matched the simulations achieving 98.2% expected in one case and 86.2% in the other. What did not match the simulations was the influence of other forces on the actuation - in this case, the gravity. Better defining this influence is paramount in future simulation of this type of blade actuation.

Having obtained correlation in the actuation simulated and measured, larger scale FEM simulations were run, with different actuators setups, and a blade more representative of the UH-60A blade structure. These results concluded that this type of twist actuation is not strong enough for the optimization requirements, even without the influence forces would have on the actuation.

References

- [1] A.Pagano, S.Ameduri, V.Cokonaj, A.Prachar, Z.Zachariadis, and D.Drikakis. Helicopter blade morphing strategies aimed at mitigating environmental impact. *Journal of theoretical and applied mechanics*, 49:1233–1259, 2011.
- [2] M.Lonoce. Helicopter blade twist optimization in forward flight. Master’s thesis, Instituto Superior Técnico, 2016.
- [3] C.S.Patil, S.Roy, and K.R.Jagtap. Damage detection in frame structure using piezoelectric actuator. *Materials Today: Proceedings*, 4:687–692, 2017. 5th International Conference of Materials Processing and Characterization.
- [4] Z.Zhang, H.Xiang, Z.Shi, and J.Zhan. Experimental investigation on piezoelectric energy harvesting from vehicle-bridge coupling vibration. *Energy Conversion and Management*, 163:169–179, 2018.
- [5] A.Franzini, F.Legnani, E.Beretta, F.Prada, F.DiMeco, S.Visintini, and A.Franzini. Piezoelectric surgery for dorsal spine. *World Neurosurgery*, 114:58–62, 2018.
- [6] M.L.Wilbur, P.H.Mirick, Jr W.T.Yeager, C.W.Langston, C.E.S.Cesnik, and S.J.Shin. Vibratory loads reduction testing of the nasa/army/mit active twist rotor. *Journal of the American Helicopter Society*, 47:123–133, 2002.
- [7] D.Dwarakanathan, R.Ramkumar, S.Raja, and P.S.S. Rao. Design, development and ground testing of hingeless elevons for mav using piezoelectric composite actuators. *Advances in Aircraft and Spacecraft Science*, 2:303–328, 2015.
- [8] O.Bilgen. Macro fiber composite actuated unmanned air vehicles: Design, development, and testing. Master’s thesis, Virginia Polytechnic Institute and State University, 2007.
- [9] O.Bilgen. *Aerodynamic and Electromechanical Design Modeling and Implementation of Piezo-composite Airfoils*. PhD thesis, Virginia Polytechnic Institute and State University, 2010.
- [10] S.Rowe, A.Riquer, O.Sosnicki, and F.Claeyssen. *New developments in piezo actuators: Long stroke actuators and high power electronics*, 2016. Symposium de Genie Electrique.
- [11] X.Yuan, Z.Chen, M.Wu, H.Luo, C.Chen, K.Zhou, and D.Zhang. A novel thickness polarized d15 shear piezoelectric fiber composites. *Sensors and Actuators A: Physical*, 260:185–190, 2017.
- [12] Smart Material Corp. *Macro Fiber Composite (MFC) brochure*, 2.3 edition.
- [13] A.A.Bent. Piezoelectric fiber composites for structural actuation. Master’s thesis, Massachusetts Institute of Technology, 1994.
- [14] W.H.Hayt Jr and J.A.Buck. *Engineering Electromagnetics, 6th edition*. McGraw-Hill, 2001.
- [15] J.N.Reddy. *Mechanics of Laminate Composite Plates and Shells: Theory and Analysis, 2nd edition*. CRC press, 2005.
- [16] M.R.Schultz. *Use of Piezoelectric Actuators to Effect Snap-Through Behavior of Unsymmetric Composite Laminates*. PhD thesis, Virginia Polytechnic Institute and State University, 2003.
- [17] J.D.Singleton and Jr W.T.Yeager. Important scaling parameters for testing model-scale helicopter rotors. *Journal of Aircraft*, 37:396–402, 2000.
- [18] Goodfellow. retrieved January 2018 from <http://www.goodfellow.com/E/Polyethyleneterephthalate.html>.
- [19] Airfoiltools. retrieved January 2018 from <http://airfoiltools.com>.
- [20] C.Bishop. *Sikorsky UH-60 Black Hawk*. Osprey Publishing, 2008.